6-15-2017

Improved Atmospheric Characterization for Hyperspectral Exploitation

Nathan P. Wurst

Improved Atmospheric Characterization for Hyperspectral Exploitation

THESIS

Nathan P. Wurst, Civilian, USAF

AFIT-ENP-MS-17-J-014

DEPARTMENT OF THE AIR FORCE
AIR UNIVERSITY

AIR FORCE INSTITUTE OF TECHNOLOGY

Wright-Patterson Air Force Base, Ohio

AFIT-ENP-MS-17-J-014

IMPROVED ATMOSPHERIC CHARACTERIZATION FOR HYPERSPECTRAL EXPLOITATION

THESIS

Presented to the Faculty

Department of Engineering Physics

Graduate School of Engineering and Management

Air Force Institute of Technology

Air University

Air Education and Training Command

in Partial Fulfillment of the Requirements for the

Degree of Master of Science in Applied Physics

Nathan P. Wurst, B.S.E.E.

Civilian, USAF

May 30, 2017

AFIT-ENP-MS-17-J-014

IMPROVED ATMOSPHERIC CHARACTERIZATION FOR HYPERSPECTRAL EXPLOITATION

THESIS

Nathan P. Wurst, B.S.E.E.
Civilian, USAF

Committee Membership:

Dr. Steven Fiorino
Chair

Dr. Joseph Meola
Member

Dr. Jack McCrae
Member

Table of Contents

List of Figures

List of Tables

Abstract

Airborne hyperspectral imaging (HSI) has shown utility in material detection and identification. Recent interest in longwave infrared (LWIR) HSI systems operating in the 7-14 micron range has developed due to strong spectral features of minerals, chemicals, and gaseous effluents. LWIR HSI has the advantage over other spectral bands by operating in day or night scenarios because emitted/reflected thermal radiation rather than reflected sunlight is measured. This research seeks to determine the most effective methods to perform model-based atmospheric compensation of LWIR HSI data by comparing results obtained from different atmospheric profiles. The standard model for mid-latitude summer (MLS) and radiosonde data are compared to the National Operational Model Archive and Distribution System (NOMADS) numerical weather predictions and the Extreme and Percentile Environmental Reference Tables (ExPERT). The two latter atmospheric profiles are generated using the Laser Environmental Effects Definition and Reference (LEEDR) software. MLS has been a standard starting point for model-based atmospheric compensation codes, but this study tests the effectiveness of starting with a more accurate model of the atmosphere. The results suggest improvements can be obtained using NOMADS and ExPERT when compared to MLS and radiosonde approaches.

IMPROVED ATMOSPHERIC CHARACTERIZATION FOR HYPERSPECTRAL EXPLOITATION

I. Introduction

Two common forms of remote sensing are imaging and spectrometry. Imaging focuses electro-optical signals from a scene onto a focal plane array to collect intensity information related to spatial coordinates in the scene, while spectrometry uses dispersive optics to separate signals into their wavelength components to determine the intensity at each wavelength. These two sensing techniques are combined to form hyperspectral remote sensing. A traditional dispersive hyperspectral imager focuses a scene onto a slit, which is then dispersed into wavelength components and focused onto a focal plane array. The data collected during one measurement contains a spatial dimension along the slit and a spectral dimension along the dispersion direction. The slit is then scanned across the scene to build a second spatial dimension. The resulting data cube contains a spatial image of the scene at generally 100-200 different wavelengths [13].

Hyperspectral imagers (HSI) are often used on airborne platforms and have shown utility in material detection and identification. Recent interest in longwave infrared (LWIR) HSI systems operating in the 7-14 micron range has developed due to strong spectral features of minerals, chemicals, and gaseous effluents. LWIR HSI has the advantage over other spectral bands by operating in day or night scenarios because LWIR sensors measure emitted and reflected thermal radiation rather than reflected sunlight.

The goal of LWIR HSI is to remotely extract an object's emissivity, or transmission

and absorption for gasses, for target identification or detection. This process is done in two steps: atmospheric compensation, and temperature and emissivity separation.

Atmospheric compensation can be performed using in-scene methods such as quick atmospheric compensation (QUAC) [9], in-scene atmospheric compensation (ISAC) [29], autonomous atmospheric compensation (AAC) [19], empirical line method (ELM) [13], adaptive empirical line method (AELM) [5], and emissive empirical line method (EELM) [12]. These methods use some a priori knowledge of the scene to calculate linear offset and scaling spectra that represent the effect of the atmosphere for each pixel. There are also model-based atmospheric compensation solutions such as fast line-of-sight atmospheric analysis of spectra hypercubes (FLAASH) [22], its infrared counterpart FLAASH-IR [4], and Oblique Projection Retrieval of the Atmosphere (OPRA) [26] that use radiative transfer models to estimate path transmission, upwelling radiance, and downwelling radiance. These are then passed into a temperature and emissivity separation algorithm to extract an estimate of the targets emissivity [10], [11].

For many applications, an integrated downwelling sky radiance is sufficient to represent downwelling radiance, and gives accurate emissivity results. For low emissivity non-lambertian targets, directional downwelling radiance data may be required to get accurate results. A target of this type may reflect cold portions of the sky in nadir viewing geometries or warm portions of the sky and background in non-nadir or tilted object configurations [28]. These downwelling radiances are not represented well by integrated sky radiance. Using an integrated sky in these scenarios can result in unphysical temperature retrieval and spectral artifacts in the emissivity approximations. A more complete hemispherical model of the sky downwelling radiance is necessary to retrieve accurate emissivity for a broader class of materials and imaging scenarios. One of the most commonly used radiative transfer tools in the HSI community is the

moderate spectral resolution transmittance code, or MODTRAN [28].

MODTRAN is a set of radiative transfer codes that have been continuously developed and updated by Spectral Sciences, Inc. and the Air Force Research Laboratory for over 25 years. MODTRAN breaks the atmosphere into horizontal layers to do line of sight path transmission and path radiance calculations with a user-selectable radiative transfer algorithm. These calculations can be done over spectral ranges from the ultraviolet to the LWIR [7]. MODTRAN offers pre-made standard atmospheric profiles and allows the user to vary the parameters of these models in order to better represent the atmosphere in a specific scenario. Users can also input radiosonde or climatology data for a more accurate atmospheric model [6].

MODTRAN and other radiative transfer models are used in model-based atmospheric compensation algorithms to correct LWIR HSI data. MODTRAN allows the user to define the atmosphere at the time of collection and uses that atmospheric profile to model the downwelling radiance, upwelling radiance, and path transmission. Radiative transfer modeling tools excel in situations where ground truth information about in-scene material emissivity is difficult or impossible to collect [13].

The Laser Environmental Effects Definition and Reference (LEEDR) code is a verified and validated, fast-calculating, first principles atmospheric characterization and radiative transfer package developed at the Air Force Institute of Technology (AFIT). It enables the creation of vertical profiles of temperature, pressure, water vapor content, optical turbulence, and atmospheric particulates as they relate to line-by-line layer extinction coefficient magnitude at any wavelength from the ultraviolet to radio frequencies. In addition to its broad spectrum of consideration, LEEDR uniquely allows for a temporally and spatially varying atmospheric boundary layer (approximately the lowest 1500 m of the atmosphere) through the use of its correlated, probabilistic databases in the production of its vertical profiles of data. This

allows LEEDR to produce profiles of meteorological data and effects that could actually occur or have actually occurred at a particular location and time, and attach the statistical likelihood of such occurrence for that time and place. This differs significantly from using standard atmospheric profiles (e.g. the U.S. Standard Atmosphere, 1976) in engineering analyses or simulations [16]. Additionally, a National Oceanic and Atmospheric Administration (NOAA) Operational Model Archive Distribution System (NOMADS) data feed has been incorporated to supply observations or real-time numerical weather prediction (NWP) forecasts (out to 180 hours) for use in profile generation [15].

The primary difference between using MODTRAN and LEEDR for atmospheric compensation of hyperspectral imaging is that LEEDR allows the user to generate accurate atmospheric profiles for the times and locations of the measurements rather than relying on standard atmospheres, or forcing the user to import properly format radiosonde data, climatology data, or NWP data. The user can define specific atmospheric conditions with more fidelity than MODTRAN can offer. Because radiosonde and climatology data are not always available, LEEDR gives more flexibility in terms of atmospheric characterization [27].

The goal of this thesis is to determine if using LEEDR's atmospheric modeling tools for atmospheric compensation of LWIR HSI data provides some quantitative benefit over using standard atmospheres such as MLS. First, LEEDR will be used to generate NOMADS and ExPERT atmospheric models for each HSI data cube. MODTRAN will be used to generate transmission, upwelling radiance, and downwelling radiance spectra to use for atmospheric compensation. Target emissivity will be extracted using known temperatures rather than using a temperature/emissivity separation algorithm. The extracted emissivities will be compared to truth spectra using root-mean-square error and standard deviation of the residual. The NOMADS

and ExPERT atmospheric profiles are expected to result in less error than the standard atmosphere.

II. Background

In 1966, a collaboration between the University of Michigan and Purdue University resulted in the first multispectral sensor. The goal was to produce a sensor that could measure health and growth of crops in the agricultural industry. The sensor could capture data from the visible to the LWIR in up to eighteen different spectral bands. This technology grabbed the attention of other research institutions. By 1968, the National Aeronautics and Space Administration (NASA) began working on the sensor known as Landsat, the first space based multispectral imaging platform [21].

Multispectral images are made up of a collection of broadband images, each in a different spectral band. These images can then be analyzed as a group to differentiate objects in the scene. Many times, three of the spectral bands are combined into one image to create a pseudocolor image. This technique allows for easy visual analysis of the data. Using multiple spectral bands adds a third dimension over standard imagery by providing spectral information along with spatial information [13]. This technology was proven useful in 1971 when the Indiana corn crop was attacked by a fungus. Multispectral imaging was able to detect which fields were infected, what stage the infection was, and the health of the crop.

Hyperspectral imaging was developed from multispectral imaging, but driven by the desire for higher spectral resolution [21]. Hyperspectral imaging is defined by the acquisition of images in hundreds of contiguous spectral bands such that for each pixel a radiance spectrum can be measured. Because the spectral bands are contiguous, hyperspectral imaging is able to spatially and spectrally identify materials in a scene using their respective spectral signature. For imaging scenarios when material identification rather than discrimination is key, hyperspectral imaging is the best option.

Hyperspectral imaging was originally developed in the private sector for Earth

remote sensing, specifically geological mapping [18]. The ability to spectrally identify minerals and plants in the visible to near IR spectrum made this field of science much easier by being able to characterize large areas in a short period of time. As the technology grew, more scientific communities started adopting HSI and it is now a staple in many remote sensing fields such as agriculture, vegetation science, urban mapping, and land use monitoring to name a few. The technology has made its way into government agencies as well with law enforcement and military applications being realized.

There are four main spectral regions that are used in HSI. The visible to near IR (VNIR, 0.35-1.0μm) , short wave infrared (SWIR, 1.0-2.5μm), mid wave infrared (MWIR, 3-5μm), and LWIR (7-14μm). VNIR and SWIR measure reflected solar radiance, LWIR measures thermal radiance, and MWIR measures a combination of the two [13]. HSI is most commonly used in the VNIR and SWIR due to maturity and lower cost, but there has recently been a growing interest in the LWIR spectrum [28]. Measuring thermal radiation rather than reflected sunlight as in the VNIR and SWIR gives advantages as well as disadvantages. Objects emit thermal radiation at all times of day allowing for collection of LWIR data during the day or night. Unfortunately, because LWIR HSI systems detect thermal energy, they generally must be cooled to cryogenic temperatures to reduce noise from instrument self emission. LWIR systems are generally higher cost and less mature than VNIR and SWIR systems [13], [28], [27].

The technology of hyperspectral imaging closely follows the development of computers, data storage, and electronics technology. Collecting imagery with fine enough spectral resolution requires fast computing and large data storage capabilities. Some of the first hyperspectral sensors used a focal plane array that was only thirty-two by thirty-two detector elements. As microfabrication techniques improved, focal planes

gained more detector elements and computing speed became faster. This, combined with better electronic data storage, allowed HSI to grow to where it is today [18].

Most dispersive HSI sensors are built in a very similar way. The incident radiation passes through a slit, which is imaged onto a dispersive optical element such as a prism or diffraction grating. The dispersed radiation is then imaged onto a focal plane array. The focal plane array is placed such that each column of pixels records a single slit image. The number of pixel columns on the focal plane determines the number of spectral bands recorded in each image. Each image taken with the sensor includes one spatial dimension along the length of the slit and one spectral dimension across many different wavebands [13].

In order to include the second spatial dimension the slit must be scanned across the scene. For ground-based sensors this can be done by scanning a mirror while taking frames, or scanning the sensor itself. For airborne sensors, more options exist. Pushbroom scanning involves aiming the sensor's slit length to be oriented perpendicular to the aircraft's direction of flight. The frame rate of the sensor is determined by the speed of the aircraft. Whiskbroom scanning orients the slit parallel to the direction of movement and uses a mirror and gimble to scan perpendicular to the direction of the aircraft's flight. This method of measurement allows for more freedom in choosing camera operating parameters, but is more difficult to implement [13], [25].

The data collected is represented as a three dimensional array, called a data cube. Because data cubes contain spatial and spectral information, special techniques have been developed for analyzing them depending on the application. Generally, each spatial pixel is treated as a single element while its corresponding spectral data is the vector of information being considered [13].

Before any analysis can be done, the data must be calibrated. There are two forms of calibration for HSI systems, spectral and radiometric. In order to know the

radiance values rather than digital counts collected by the instrument, an absolute radiometric calibration is performed. This is done using a calibrated light source for the VNIR/SWIR spectral bands or a blackbody in the LWIR. At least two measurements are required for calibration, one being a light source dimmer that the scene being measured or a blackbody colder than the scene and a light source brighter or hotter than the scene. Detectors are designed to behave linearly within their region of operation, so a line is fit to the digital counts measured from the calibration sources. Since the radiance values of the calibration sources are known, the digital counts measured in the scene can be converted to radiance values in post-processing. Spectral calibration uses gas discharge lamps to quantify the spectral alignment of the instrument. The known emission lines of the various gas lamps used are measured and can reveal detector misalignments, called "keystone", or aberrations that cause the lines to be warped, called "smile." This information shows the spectral bandwidth of each detector on the focal plane so that the post processing and analysis can be done [13], [25].

In order to make sense of HSI data, it is important to know the radiative transfer equations that model how energy makes its way to the sensor. Radiance at the sensor can be represented using a simplified diffuse facet model such that

$$L_p(\lambda) = \tau_a(\lambda)[1 - \rho_a(\lambda)]B(\lambda, T) + \frac{\tau_a(\lambda)\rho_a(\lambda)}{\pi}[E_s(\lambda) + E_d(\lambda)] + L_a(\lambda). \quad (1)$$

L_p is defined as pupil plane radiance, τ_a is transmission of the atmosphere along the sensor-to-ground path, ρ_a is reflectance of the material, and $B(\lambda, T)$ is the blackbody radiance function where T is the material surface temperature. $E_s(\lambda)$ represents the direct solar irradiance, while $E_d(\lambda)$ is the integrated downwelling radiance from indirect sources such as emission and scattering from the atmosphere and nearby objects [13]. Finally, $L_a(\lambda)$ is the radiance emitted from and scattered off of the atmosphere

between the sensor and the scene. This equation makes the assumption that the scene is lambertian and is therefore independent of viewing angle. If a directionally dependent answer was desired, Eq. (1) can be expressed using a bidirectional reflectance distribution function (BRDF) which models the surface of a material and its directional reflectance properties. The lambertian assumption is used in practice because BRDFs are difficult to model and computationally expensive.

In the VNIR and SWIR spectral bands reflected radiance dominates emission, so for these bands Eq. (1) can be simplified to

$$L_p(\lambda) = \frac{\tau_a(\lambda)\rho_a(\lambda)}{\pi}[E_s(\lambda) + E_d(\lambda)] + L_a(\lambda). \tag{2}$$

In the LWIR, the direct solar irradinace component can be ignored, reducing Eq. (1) to

$$L_p(\lambda) = \tau_a(\lambda)[1 - \rho_a(\lambda)]B(\lambda, T) + \frac{\tau_a(\lambda)\rho_a(\lambda)}{\pi}E_d(\lambda) + L_a(\lambda) \tag{3}$$

where the value of $1 - \rho_a(\lambda)$ is assumed to be equal to emissivity, which assumes that all materials are optically opaque. These models are made for solid objects, but others exist for gaseous effluents and objects under water. Equations (2) and (3) show how all parts of the atmosphere can greatly affect a signal being measured with an HSI system [13]. In order to remove those affects, atmospheric compensation must be performed on the data.

There are two main categories of atmospheric compensation methods applied to HSI data, in-scene and model-based. In-scene methods generally use known material with a known reflectance in the scene to estimate the atmospheric transmission, upwelling radiance, and downwelling radiance (TUD) terms. A simple in-scene atmospheric compensation known as the empirical line method is performed using a linear relationship between measured radiance and known spectra [13], [12]. Gain and offset

coefficients of the atmosphere can be calculated at each spectral band. Solving for reflectance spectra, the gain and offset are removed from the HSI datacube. The transmission and irradiance terms in Eq. (2) are simplified to a single coefficient as

$$L_p(\lambda) = a(\lambda)\rho(\lambda) + b(\lambda), \tag{4}$$

where $a(\lambda)$ is the atmospheric gain and $b(\lambda)$ is the offset [13]. With at least two surface reflectance spectra measured being known, a linear regression can be performed to calculate the gain and offset.

Two radiance measurements represented as $L_1(\lambda)$ and $L_2(\lambda)$ along their two known reflectance spectra, $\rho_1(\lambda)$ and $\rho_2(\lambda)$ are used to estimate the gain and offset created by the atmosphere. A slope-intercept relationship is used such that

$$\hat{a}(\lambda) = \frac{L_2(\lambda) - L_1(\lambda)}{\rho_2(\lambda) - \rho_1(\lambda)} \tag{5}$$

and

$$\hat{b}(\lambda) = \frac{L_1(\lambda)\rho_2(\lambda) - L_2(\lambda)\rho_1(\lambda)}{\rho_2(\lambda) - \rho_1(\lambda)}. \tag{6}$$

Once the gain and offset are estimated, the reflectance spectra of the datacube can be calculated for each pixel as

$$\hat{\rho}(\lambda) = \frac{L_p(\lambda) - \hat{b}(\lambda)}{\hat{a}(\lambda)}. \tag{7}$$

This method works well in the visible spectrum, but for LWIR data the target temperature and emissivity spectra must be known rather than just the reflectance spectra [13]. There have been a few algorithms based on the ELM created for the MWIR/LWIR spectrum such as the emissive empirical line method (EELM) [12] and autonomous atmospheric compensation (AAC) [19].

Model-based atmospheric compensation methods use some radiative transfer model such as MODTRAN or LEEDR to estimate the atmospheric transmission, path radiance, downwelling radiance, and solar irradiance present in a hyperspectral measurement. These estimates are made iteratively or as a basis set to find the atmospheric parameters that fit the data best in some sense [13], [26]. All radiative transfer models require information about the atmosphere to make an accurate estimate of the modeled radiance, but the amount of variables involved in defining the atmosphere makes for an impractical problem. In the LWIR, many atmospheric parameters have similar impacts on the radiance and transmission values and can therefore be set to some "default" value that makes sense in each particular situation. The parameters that are varied include temperature, water content, and ozone. Minimizing the number of variables to iterate over increases the tractability of model-based atmospheric compensation methods [13].

Fast line-of-sight atmospheric analysis of spectral hypercubes (FLAASH) is a model based atmospheric compensation method that includes more complicated atmospheric behavior, such as multiple scattering and clouds [22]. It was originally developed for the VNIR and SWIR spectral bands but was later adapted to the MWIR and LWIR in an algorithm called FLAASH-IR. This atmospheric compensation algorithm begins by modeling the pupil plane spectral radiance as

$$L_p(\lambda) = \tau_a(\lambda)\epsilon(\lambda)B(\lambda, T) + [1 - \epsilon(\lambda)]L_d(\lambda) + L_a(\lambda). \tag{8}$$

This equation is another form of the simplified diffuse facet model in Eq. (1), where the irradiance terms were converted to a single term that represents the total downwelling radiance at the pupil plane such that

$$L_d(\lambda) = \frac{\tau(\lambda)[E_s(\lambda) + E_d(\lambda)]}{\pi} \tag{9}$$

and the reflectance terms $\rho(\lambda)$ are represented as $[1 - \epsilon(\lambda)]$ where $\epsilon(\lambda)$ is spectral emissivity [4]. This relationship between reflectance and emissivity assumes that there is no transmission and that absorption and emission are equal. Multiple scattering and clouds are included in this downwelling radiance term by modeling $E_s(\lambda)$ with more blackbody like structure for clouds and modeling $E_d(\lambda)$ to include surrounding object emission such as trees or buildings.

The FLAASH-IR algorithm starts by making arrays of scaling constants for atmospheric water content, temperature near the ground, and ozone. These scaling constants are used to adjust their respective atmospheric constituents in a standard MODTRAN atmosphere. The algorithm then uses all combinations of the scaling constants to create a library of possible atmospheres using MODTRAN. Each possible atmosphere contains a path transmission, path radiance, and downwelling radiance. Then, polynomial fitting is used to interpolate additional atmospheres between the models for finer sampling.

A set of possible emissivity spectra are estimated for each modeled atmosphere such that

$$\hat{\epsilon}(\lambda) = \frac{L_p(\lambda) - \hat{L_d}(\lambda) - \hat{L_a}(\lambda)}{B(\lambda, \hat{T})\hat{\tau}(\lambda) - \hat{L_d}(\lambda)}, \tag{10}$$

where $L_p(\lambda)$ represents the measured radiance and the estimated quantities are denoted with a hat. Each set of emissivities is estimated using a single atmosphere and a range of possible surface temperatures in the blackbody function $B(\lambda, T)$ [4]. The smooth-emissivity criterion states that the most likely solution is the emissivity spectrum with the least amount of fine spectral structure. In the LWIR, most solids have broad spectral changes while atmospheric constituents tend to have fine structure. Therefore, more fine structure is correlated to less atmosphere removed from the spectra [11].

A metric for the amount of fine spectral structure is calculated using a mean

squared residual between the measured spectrum and a modeled spectrum created using Eq. 8 and a smoothed emissivity spectrum. The emissivity is smoothed using a running average over a specified number of adjacent spectral channels. The mean squared residual is represented as

$$\sigma^2 = [L_p - \hat{L_p}(\langle\epsilon\rangle)]^2, \tag{11}$$

where

$$\hat{L_p}(\langle\epsilon\rangle) = \hat{\tau_a}(\lambda)\langle\epsilon\rangle B(\lambda, \hat{T}) + [1 - \langle\epsilon\rangle]\hat{L_d}(\lambda) + \hat{L_a}(\lambda). \tag{12}$$

The quantity σ^2 is the mean squared residual and $\langle\epsilon\rangle$ is the smoothed emissivity spectra such that

$$\langle\epsilon_k\rangle = \frac{1}{N}\sum_{n=-1}^{1}\epsilon_{k+n} \tag{13}$$

for a three band average [4], [11]. The FLAASH-IR algorithm uses a downhill simplex method to minimize the mean squared residual using a one dimensional search for surface temperature within a three dimensional search for atmospheric water, temperature near the ground, and ozone scaling constants.

This mean squared residual minimization is done on a number of different pixels (usually 10-20) in the hyperspectral image over a diverse range of brightness and emissivity spectra to ensure an accurate atmospheric retrieval for all pixels. The FLAASH-IR algorithm assumes that the atmosphere across the image is constant. Once the atmospheric retrieval is complete, the atmosphere is removed from all pixels in the image using Eq.(10) and each pixel undergoes the mean squared residual minimization to separate the temperature and emissivity out of the target leaving radiance term [4], [10].

In order to model the TUD terms, MODTRAN starts with one of its standard atmospheres. The standard atmospheres were created in 1962 by the Environmental

Science Services Administration (ESSA), the National Aeronautics and Space Administration (NASA), and the United States Air Force (USAF) for use in scientific calculations and studies of the effect of the atmosphere on aerospace vehicle design. The standard atmospheres were later updated in 1976 to provide more accurate profiles above 50km in altitude. These standard atmospheres are matrices whose columns contain altitude, temperature, pressure, and density and mixing ratios for H_2O, O_3, CH_4, and N_2O [1], [2], [3].

MODTRAN models the atmosphere as a set of spherical layers around the Earth. Each layer Z_j has two boundaries defined at altitudes z_1 and z_2. Each layer has a set of atmospheric parameters such as temperature, pressure, and molecular species densities that MODTRAN uses to calculate the TUD parameters. These atmospheric parameters are stored in standard atmosphere profiles, mid-latitude summer and tropical for instance, or can be provided by the user as a custom atmosphere profile. The profiles contain all necessary information at each layer altitude [14], [8].

MODTRAN calculates the TUD parameters in two different ways, line-by-line or statistical band model. The line-by-line method calculates the absorption by each molecular transition listed in the HITRAN database at every layer. This allows the spectra to be sampled very fine, but is computationally expensive and can take a long time to complete. The band model uses approximations to estimate the absorption in each spectral band. This method uses coarser spectral sampling, but is much faster than line-by-line and the sampling is adequate for HSI atmospheric compensation. The statistical band model was used in this research [14], [23].

In the statistical band model, MODTRAN calculates the transmittance through the atmosphere by first looking at molecular species transmittance for a single atmospheric layer. Transmission is split into three components, line center, tail, continuum. A pseudo line strength distribution for a homogeneous path is defined by n_s identical

strong lines of strength S_s with transition frequencies randomly distributed within each spectral bin and n_w identical weak lines with corresponding strength S_w. The combined transmittance from the collection of n randomSly distributed identical lines is equal to the average spectral band transmittance of a single line, t_{sl}, raised to the n^{th} power such that

$$\langle t_{total} \rangle = t_{sl}^{n}. \tag{14}$$

This is applied to the modeled strong and weak lines as

$$\langle t_{total} \rangle = t_{sl}^{n_s} \times t_{sl}^{n_w}. \tag{15}$$

The transmittance of a single line can be calculated using Beer's law as

$$t_{sl}(Su, \gamma_c, \gamma_d; \Delta\nu, D) \equiv \frac{1}{\Delta\nu} \int_{D-\Delta\nu/2}^{D+\Delta\nu/2} \exp[-Suf_\nu(\gamma_c, \gamma_d)]d\nu, \tag{16}$$

using line strength S, path column density u, collision (Lorentz) half width γ_c, Doppler half width γ_d, spectral bin width $\Delta\nu$, and the offset of the transition frequency from bin center D [14]. The function $f_\nu(\gamma_l, \gamma_d)$ is the Voigt profile defined by the collision and Doppler half widths such that

$$f_\nu(\gamma_c, \gamma_d) = \frac{\gamma_c}{\pi^{3/2}} \int_{-\infty}^{\infty} \frac{\exp(-x^2)}{\gamma_c^2 + (\nu - \gamma_d x)^2} dx. \tag{17}$$

The integral of a Voigt profile does not have an analytical form, so the single line transmittance function in Eq. (16) is expanded into an expression in terms of modified Bessel functions. By modeling the line distribution as identical strong and identical weak lines the Voight profile only needs to be computed twice, reducing computation time [14], [8].

Next, MODTRAN defines the line center displacement D from bin center. Mod-

eling the line to be in the center of the bin creates a bias towards more absorption. An average single-line spectral band transmittance is desired. Correctly spaced lines have a spectral transmittance equal to the mean transmittance of a transition whose center is randomly distributed in the spectral bin. Determining line center location is difficult for a Voigt molecular transition. For pure Lorentzian conditions, $\gamma_d = 0$ cm^{-1} in the weak line limit, u is small and $\exp(-Suf_n u) \approx 1 - Suf_\nu$. The exact analytic expression for the offset from bin center $D = D_{\Delta\nu}(r_c)$ can be derived as a function of the ratio of the Lorentz half-width to the bin width, where $r_c = \gamma_c/\Delta\nu$ such that

$$\left(\frac{D_{\Delta\nu}(r_c)}{\Delta\nu}\right)^2 = \frac{1}{4} - (1+r_c^2)\frac{1 - r_c \tan\left[r_c \ln\left(1+\frac{1}{r_c^2}\right)\right]}{2 + \left(\frac{1-r_c^2}{r_c}\right)\tan\left[r_c \ln\left(1+\frac{1}{r_c^2}\right)\right]} \tag{18}$$

[14], [23].

Next the line tails are modeled. Line tails outside the current bin but less than 25 cm^{-1} from the bin center are modeled. MODTRAN models the line tail transmittance in a spectral bin accurately using Pedé approximations, which are ratios of quadratic polynomials. They can do this because the line tails vary smoothly with at most a single minimum in a bin. There are five Padé parameters that are determined from the HITRAN database. Because the line fitting is relatively simple, the line tails are sampled coarsely and the result is interpolated to reduce computation time. The resulting line tail model is calculated to be within 0.0001 of the true transmittance [14].

Continua transmittance is different from the line center and tails in that only H_2O and CO_2 are modeled. All other molecular absorptions are insignificant when the line center is further than 25 cm^{-1} from the current spectral bin. The temperature dependent spectral absorption cross-section is calculated for H_2O by partitioning it

into a foreign and a temperature-dependent self-broadening component. The two parameters are calculated from 0 to 10,000 cm^{-1} with 5 cm^{-1} spacing and then used to calculate the total absorption cross section.The CO_2 continuum absorption cross section is easier to calculate because CO_2 has a zero dipole moment, so partitioning into two broadening components is not necessary. The CO_2 absorption cross section is also calculated from 0 to 10,000 cm^{-1} but with 10 cm^{-1} spacing [14], [8].

To calculate upwelling and downwelling radiance terms, MODTRAN defines the monochromatic radiant intensity $I_0(\Omega_0;\nu)$ in integral form as

$$I_0(\Omega_0;\nu) = e^{-\tau_\ell(\nu)} I_\ell(\Omega_\ell;\nu) + \int_0^{\tau_\ell(\nu)} e^{-\tau_{\ell'}(\nu)} J_{\ell'}(\Omega_{\ell'};\nu) d\tau_{\ell'}(\nu), \tag{19}$$

where $I_0(\Omega_0;\nu)$ is radiant intensity, ν is spectral frequency, and Ω_0 is sensor view direction. The subscript ℓ denotes path length. Equation 19 states that the observed spectral radiant intensity at the sensor is the sum of two terms. The first is the spectral radiant intensity directed toward a sensor along path length ℓ and attenuated by atmospheric transmittance along that same path. The second term is the path radiance, equal to the LOS integral over the source radiation $J_{\ell'}(\Omega_{\ell'};\nu)$ directed toward the sensor and attenuated by the transmittance.

The band model computes radiative transfer quantities integrated over narrow spectral bins. The radiant intensity measured at a sensor, $\langle I_0(\Omega)\rangle$, is defined by

$$\langle I_0(\Omega)\rangle \equiv \frac{1}{\Delta\nu} \int_{\Delta\nu} I_0(\Omega;\nu) d\nu, \tag{20}$$

where $\Delta\nu$ is the spectral bin width. The upwelling and downwelling spectra are calculated using these two equations and the computed atmospheric transmittance [14].

As previously noted, Laser environmental effects definition and reference (LEEDR)

is a tool created by the Air Force Institute of Technology. LEEDR and MODTRAN operate in a similar fashion, but LEEDR includes a tool for generating realistic atmospheric profiles rather than relying on standard atmospheric profiles. The ability to model atmospheric profiles based on numerical weather prediction (NWP) data or correlated probabilistic climatology rather than starting with a standard atmosphere as in MODTRAN could reduce computation times and provide the ability to calculate an atmosphere that is close to the true atmosphere at the time of data collection.

There are two ways that LEEDR models atmospheric profiles, the first is by using the Extreme and Percentile Environmental Reference Tables (ExPERT) database and the second is using the National Operational Model Archive and Distribution System (NOMADS). The ExPERT database contains data from 573 land sites around the world with surface data of temperatures, pressures, relative humidities, and more. Probabilistic climatological atmospheric profiles are developed using the ExPERT data coupled with regional upper air climatologies. Atmospheric profiles for all locations can be produced using NWP data in the NOMADS database. The NOMADS database, managed by the National Oceanic and Atmospheric Administration (NOAA), is a database where communities can upload weather data to a secure Internet server for public distribution. Data from various NWP models is available including Climate Forecast System, North American Regional Reanalysis, Global Ensemble Forecast System, Navy Operational Global Atmospheric Prediction System, CM2 Global Coupled Climate Models, and many more. It contains NWP data and latitude/longitude interpolation for an accurate representation of the atmosphere at almost any location across the globe [15], [16], [17], [24].

III. Experiment

The goal of this research is to determine if using LEEDR's atmospheric modeling capabilities provides a significant advantage to using standard atmospheric profiles in model-based atmospheric compensation of HSI data. The data used for this work were collected using the Spatially Enhanced Broadband Array Spectrograph (SEBASS) LWIR sensor on an airborne platform at 9,000, 6,000, and 3,000 feet above

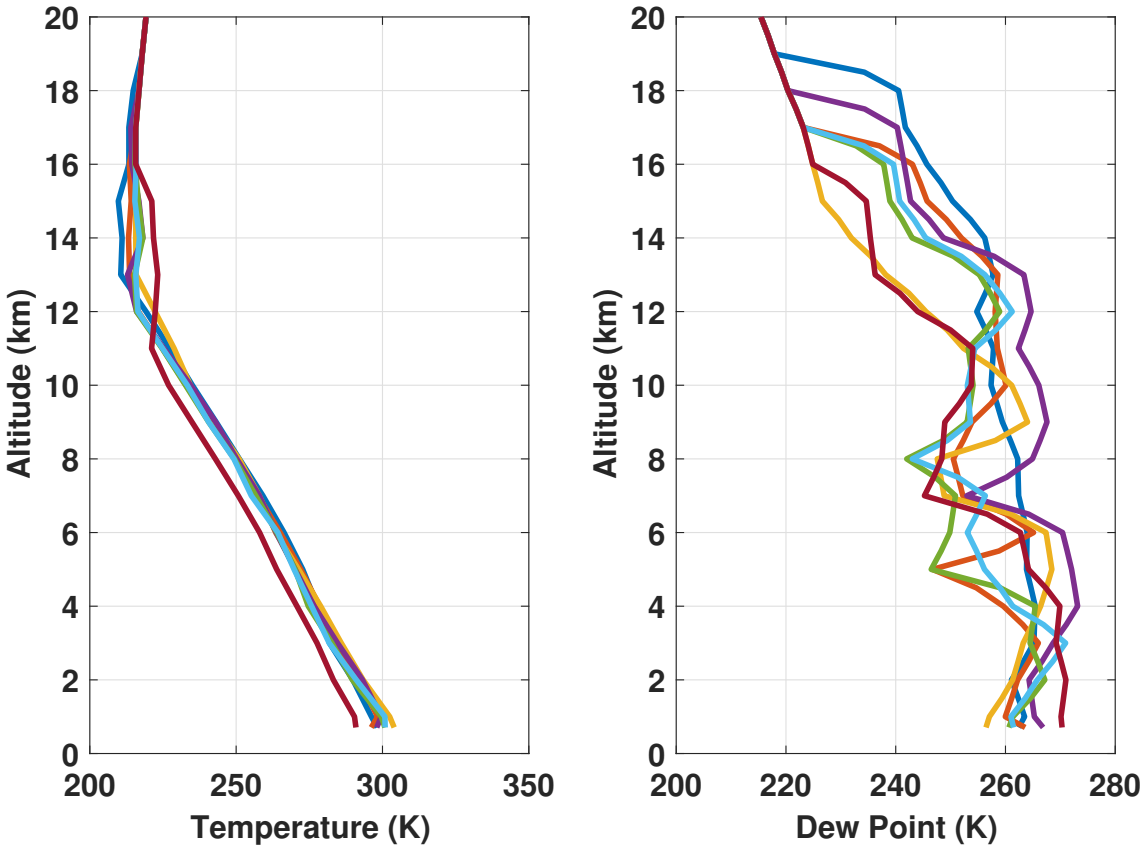

(a) Temperature

(b) Dew Point

Figure 1. 1a and 1b plot the temperature and water content respectively of the radiosonde measurements used in the atmospheric compensation of each data cube to show the diversity in weather conditions between the data sets. The ground temperature varies from 290.9K to 304K and the surface dew point varies from 256.5K to 270.3K.

ground level. The data used was collected between August 11 and August 20 of 2014

at a location considered to be within the mid-latitude region. Targets of varying size, emissivity, tilt geometry, surface roughness, and surface temperature were collected, but for the purpose of this research only four targets were examined: low emissivity paint, medium emissivity paint, high emissivity black paint, and high emissivity white paint. Each target had thermocouples attached which logged temperature measurements once per minute. A mobile weather station was used to log surface weather conditions once every two minutes. Ground truth emissivity signatures were were obtained from field measurements using a Designs and Prototypes (D&P) Fourier transform infrared spectrometer.

Seven different data cubes were used for this research. Figure 1 plots the temperature and water content of the radiosonde measurements used in the atmospheric compensation of each data cube to show the diversity in weather conditions between the data sets. The ground temperature varies from 290.9K to 304K and the surface dew point varies from 256.5K to 270.3K. The diversity in dew point continues throughout the atmosphere until 19km in altitude where all of the profiles converge.

The atmospheric compensation algorithm used is similar to the FLAASH-IR algorithm in that it iterates over a set of surface temperature, water concentration, and ozone vectors using a Nelder-Mead simplex to minimize error until it finds the best possible atmospheric compensation. A group of diverse pixels are automatically selected based on large spectral variation. A library of five hundred emissivity spectra are forward modeled to pupil plane radiance using the TUD spectra. The diverse pixels are identified using this spectral library and an RMS spectral error is calculated between the modeled spectra and diverse pixel spectra. The RMS error is the metric minimized using the Nelder-Mead simplex. Gradient based minimization techniques are rarely used in atmospheric compensation algorithms because they are prone to finding local minima rather than the global minimum.

There is never a single solution to an atmospheric compensation problem. The exact atmosphere is not required to get accurate atmospheric compensation results. There are many constituents that make up different atmospheric conditions, and different combinations of these can produce very similar results when boiled down to a simple transmission, upwelling radiance, and downwelling radiance. Therefore, non-gradient techniques such as Nelder-Mead are more consistent in their results due to their ability to look past local minima.

The atmospheres are put into MODTRAN5 to generate the TUD spectra for atmospheric compensation. MODTRAN was used to perform the radiative transfer calculation in all cases because the purpose of this research is to determine the advantage of LEEDR's modeled atmospheres, and not to evaluate radiative transfer codes or temperature-emissivity separation algorithms. The TUD spectra were then used with the known target temperature to extract emissivity spectra to provide consistency in temperature/emissivity separation.

The emissivity spectra were extracted using the Lambertian reflectance model from Eq. 8. The algorithm outputs an initial set of TUD spectra, initial extracted emissivity, TUD spectra after iteration, and a final extracted emissivity. This algorithm was set to do 50 iterations on the atmospheric constraints before stopping.

There were four basic atmosphere profiles used to perform atmospheric compensation on each data cube: NOMADS NWP, ExPERT, Mid-Latitude Summer (MLS), and Radiosonde data. The NOMADS and ExPERT atmospheres were selected based on date, time, and location the data cube was collected. MLS was used as the standard atmosphere because the data were collected in a mid-latitude region. Radiosonde balloons were launched at regular intervals throughout each day of the data collection and the measurement closest in time to each data cube collection was used. The radiosonde profiles are often considered to be the best initial solution to the

atmospheric compensation because it is a measure of the atmosphere at or near the time of the collection. For experimental data collections it is considered to be the true atmosphere, but in operational scenarios it is often not possible to obtain local radiosonde measurements.

A common practice in atmospheric compensation is to correct the atmosphere profile to a known ground temperature and water content. This scenario was also tested by using the known surface temperature and relative humidity measured by the mobile weather station at the time the data were collected. Young et al present a method for adjusting the temperature profile such that

$$T_c(z) = \begin{cases} T_0 - 6.49z; & z \leq (T_0 - 216.7)/6.49 \\ 216.7; & z > (T_0 - 216.7)/6.49 \end{cases} \tag{21}$$

where $T_c(z)$ is the corrected atmospheric temperature vs altitude, T_0 is the temperature measured at the ground, and z is altitude. This parametric equation gives all temperature profiles a lapse rate of -6.49 until it reaches 216.7K where it stays for all higher altitudes.

This method presents two problems. The temperature fluctuates at higher altitudes after it reaches 216.7K, and the temperature profiles used in this research don't necessarily have the same lapse rate. The lapse rate used in Eq. 21 is specifically for the 1976 US standard atmosphere, but the change in temperature with altitude for the NOMADS, ExPERT, or radiosonde atmospheres could be different. A new

parametric equation was devised to calculate the adjusted temperature profile as

$$T_c(z) = \begin{cases} (T_0 - \tilde{T}_0) + \tilde{T}(z); & z \leq 8 \\ T_0 + \ell z; & 8 < z \leq (T_0 - 216.7)/\ell \\ \tilde{T}(z); & z > (T_0 - 216.7)/\ell \end{cases} \tag{22}$$

using an estimated lapse rate ℓ calculated from the original temperature profile $\tilde{T}_(z)$. The first 8km of atmospheric temperature is shifted based on the difference between the measured ground temperature T_0 and the profile ground temperature $\tilde{T}_0$. The lapse rate ℓ of the temperature profile is estimated and used until the temperature reaches 216.7K. The original temperature profile is then used for all altitudes above the first 216.7K, preserving the upper atmosphere temperatures and the original lapse rate.

The water concentration in parts per million by volume (PPMV) was adjusted as

$$C_{H_2O}(z) = \begin{cases} C_{H_2O}(z)[1 + (\frac{C_0}{C_{H_2O}(z_g)} - 1)(1 - e^{-0.8(16-z)})^6], & z \leq 16 \\ C_{H_2O}(z), & z > 16 \end{cases} \tag{23}$$

where C_0 is the measured surface water concentration and $C_{H_2O}(z_g)$ is the profile water concentration at the ground. This adjusts the water concentration in a way that is exponentially dependent on altitude for a smooth transition between adjusted and original profile values [29].

The extracted emissivity was compared to ground truth measurements using two error metrics, RMS error and STD of the residual. RMS error is an appropriate metric to use in judging the magnitude of the emissivity differences, and STD of the residual allows for a measure of the variation between the known and extracted spectra while omitting the mean. In target detection, some variation of correlation rather than

RMS error is used because targets orientation or temperature has a large impact on the magnitude of the retrieved emissivity. A correlation metric was not used because all target detection algorithms use a different correlation metric, and choosing one could skew the results. Also, the STD of the residual is a simple way to show spectral deviation caused by the atmospheric profiles. The RMS error was calculated as

$$\text{RMS Error} = \sqrt{\overline{[\hat{\boldsymbol{\epsilon}} - \boldsymbol{\epsilon}]^2}}, \tag{24}$$

where $\hat{\boldsymbol{\epsilon}}$ is the extracted emissivity spectra and $\boldsymbol{\epsilon}$ is ground truth emissivity spectra. The STD is then calculated as

$$\begin{aligned} \boldsymbol{\epsilon_d} &= \hat{\boldsymbol{\epsilon}} - \boldsymbol{\epsilon} \\ \text{STD} &= \sqrt{\overline{[\boldsymbol{\epsilon_d} - \overline{\boldsymbol{\epsilon_d}}]^2}}. \end{aligned} \tag{25}$$

IV. Results

All figures in this section that reference a single data cube are a result of the data cube taken 8/12/2014 at 15:12 UTC at an altitude of 9000ft, which was found to be representative of the rest of the results. For data that spans multiple data cubes, the cubes are differentiated by using the date and time the cube was collected. All displayed times are in UTC, but the local time at the collection site was six hours behind UTC. The data cube labeled 8/19/2014, 03:43 UTC was actually taken 8/18/2014, 21:43 local time. As for altitude, on the 11th, 12th, and 13th the sensor was flown at 9000ft, on the 18th the sensor was flown at 6000ft, and on the 19th and 20th it was flown at 3000ft.

Figures 2a and 2b plot the initial temperature and dew point used to perform atmospheric compensation on the data cube taken on 8/12/2014 at 15:12 and at 9000ft. The temperature and water content in the first 3km are the most influential in terms of atmospheric absorption and emission, and these atmospheric profiles show a large amount of variation. The surface temperatures range from 283.7K to 298.2K and the dew point varies from 259.6K to 268.1K.

The variation in temperature and water content close to the surface causes significant differences in the transmission, upwelling radiance, and downwelling radiance as shown in Figure 3. The temperatures and surface water content for the NOMADS and ExPERT atmospheres are less than the MLS values, which corresponds to higher transmission and lower atmosphere emitted radiance. Figures 4 and 5 show the results of these differences. Low estimated transmission with high estimated down/upwelling radiance terms lead to extracted emissivity that has a lower mean than the truth. It can be seen that the NOMADS and ExPERT atmospheres provide more accurate atmospheric compensation results compared to MLS and even the radiosonde when looking at the two high emissivity targets.

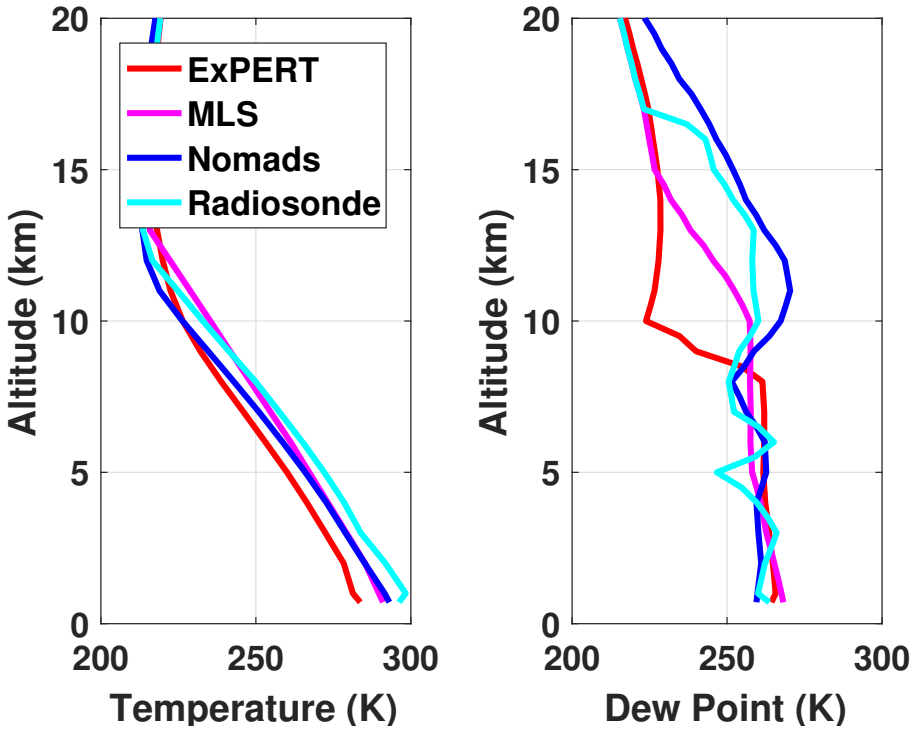

(a) Temperature (b) Dew Point

Figure 2. Figures 2a and 2b plot the four modeled temperature and dew point profiles for the data cube taken on 8/12/2014 at 15:12 UTC. The temperature and water content in the first 3km are the most influential in terms of atmospheric absorption and emission, and these atmospheric profiles show a large amount of variation. The surface temperatures range from 283.7K to 298.2K and the dew point varies from 259.6K to 268.1K.

Figure 6 shows a more quantitative difference between the extracted emissivity spectra. Figure 6a shows the RMS error of the extracted spectra for the low emissivity target, and Figure 6b shows the STD of the residual. These errors are the result of the first guess atmospheric profiles. The trend that the NOMADS and ExPERT atmospheres result in less atmospheric compensation error is consistent across all data cubes. There are two data cubes that visually stand out as having higher error values that the rest. Looking at the radiosonde data collected on 8/13/2014, there was a larger total atmospheric water content than on any other day. Also, there was sparse cloud cover throughout the day. Although data cubes were excluded from this

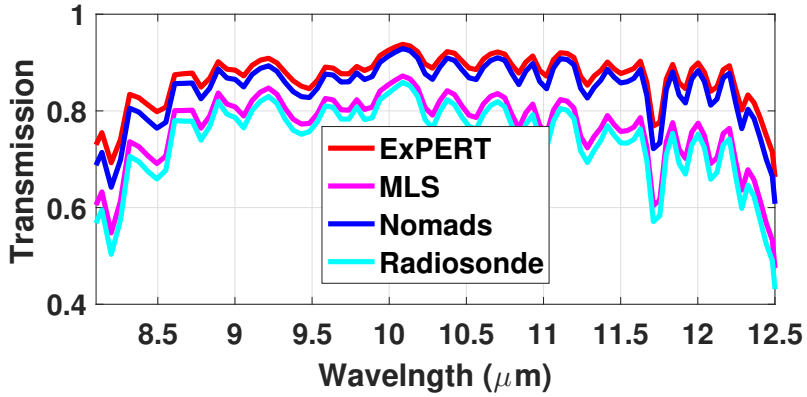

(a) Transmission

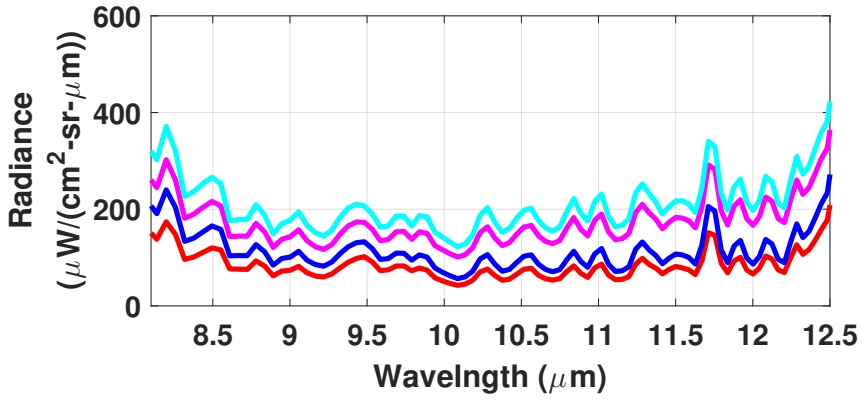

(b) Upwelling Radiance

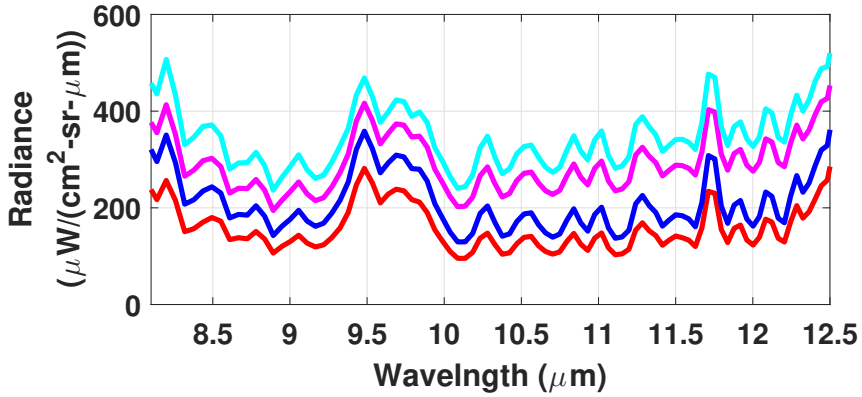

(c) Downwelling Radiance

Figure 3. Figures 3a, 3b, and 3c plot the initial guess for the transmission, upwelling, and downwelling radiance respectively. It should be noted that the NOMADS and ExPERT transmissions are higher and the upwelling and downwelling radiances are lower. This is caused by the lower temperature and water content modeled in the NOMADS and ExPERT atmospheric profiles.

study for having cumulus clouds anywhere in the sky or cirrus clouds anywhere other than the horizon regions, it is possible that some horizon cirrus clouds effected the data and caused an increase in error. The data collected on 8/19/2014 was collected at night, and the cloud cover in unknown. It is possible that sparse cloud cover effected the emissivity recovery error.

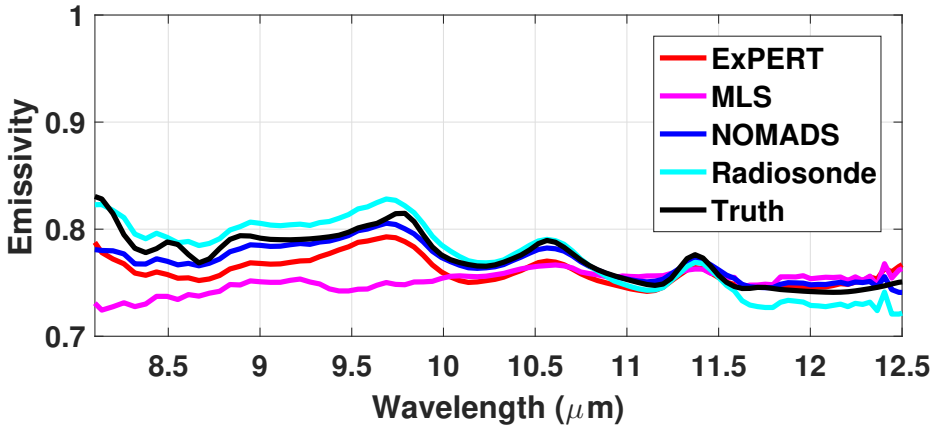

(a) Low Emissivity Target

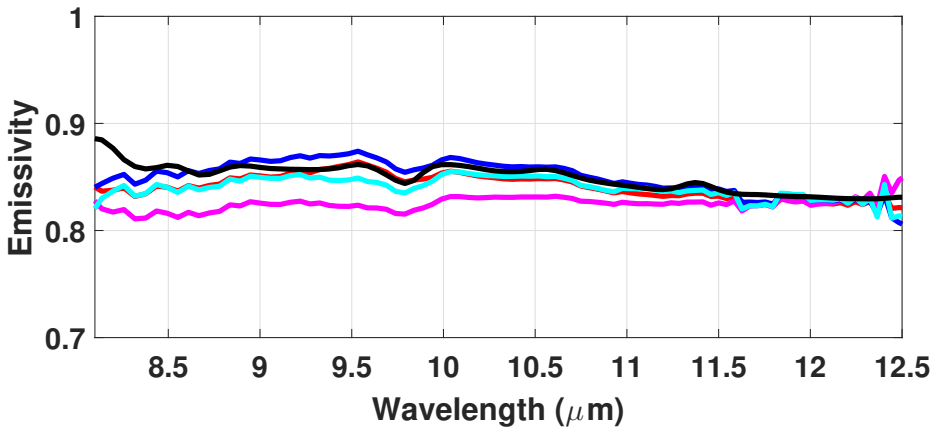

(b) Medium Emissivity Target

Figure 4. This figure shows the extracted emissivity of the low and medium emissivity target using the first guess atmospheres. It can be seen that the emissivity extracted using the MLS atmosphere does not match the spectral shape of the low emissivity target's truth and has the largest amplitude error with the medium emissivity target. Of the spectra extracted using NOMADS, ExPERT and radiosonde data, NOMADS is most accurate for the low emissivity target and ExPERT is most accurate for the medium emissivity target.

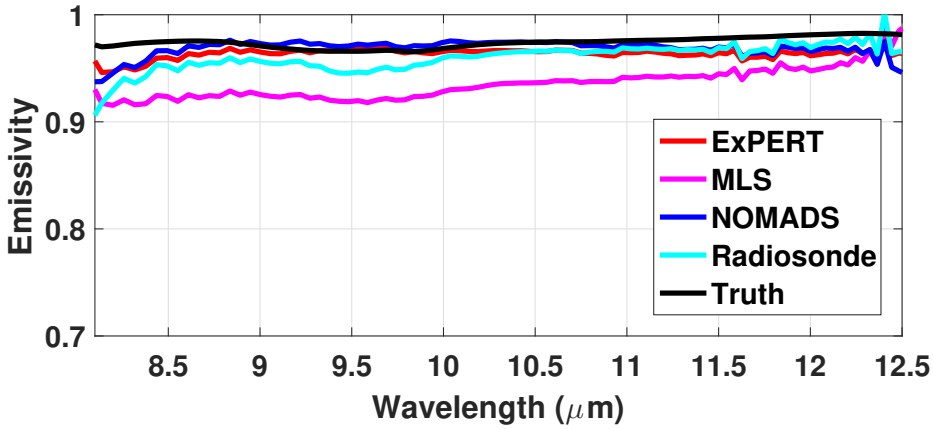

(a) High Emissivity White Target

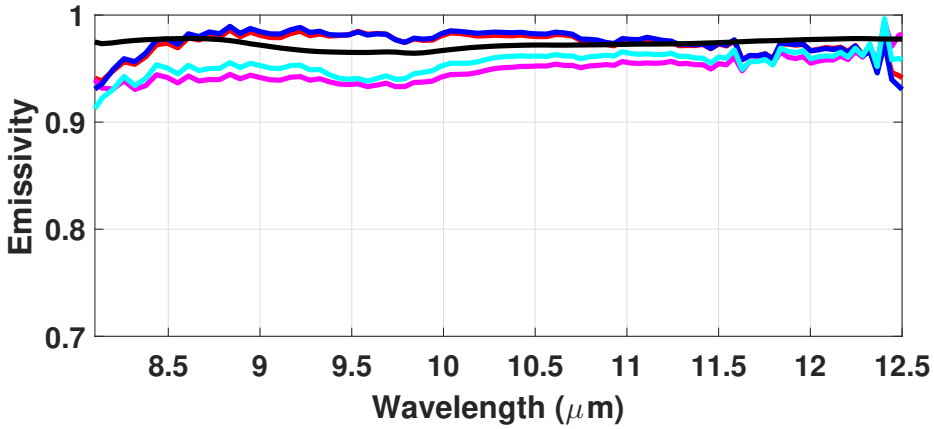

(b) High Emissivity Black Target

Figure 5. Figure showing the extracted emissivity of the two high emissivity targets using the first guess atmospheres. These spectra are much harder to correct for because of the lack of spectral features, but it is obvious that the NOMADS and ExPERT atmospheres provide a more accurate atmospheric compensation than MLS or the radiosonde in these cases.

Table 1 displays the RMS error calculated for all extracted emissivity over all data cubes, and Table 2 shows the STD of the residual. It is easily seen that the NOMADS and ExPERT atmospheres provide an advantage over MLS for this data set. Out of all the data, MLS had less RMS error than NOMADS only once, and did not have less STD at all. The average RMS error over all targets and data cubes is listed at the bottom of Table 1 along with the uncertainty of that average. The uncertainty was

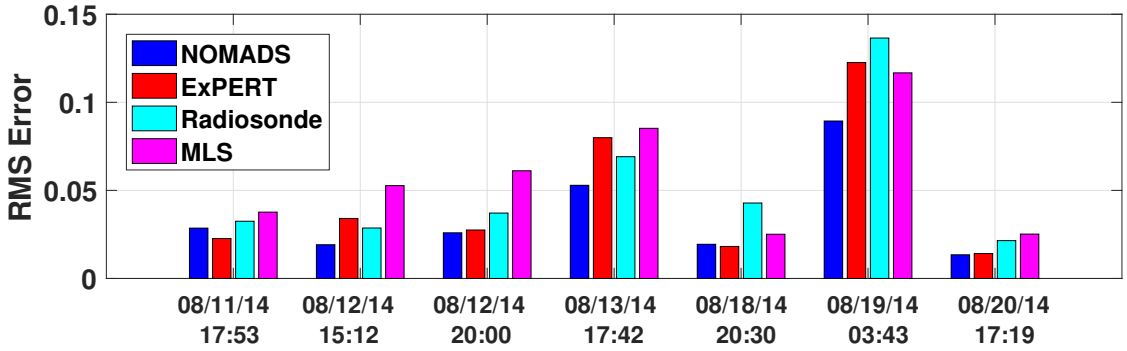

(a) RMS Error of Low Emissivity Target

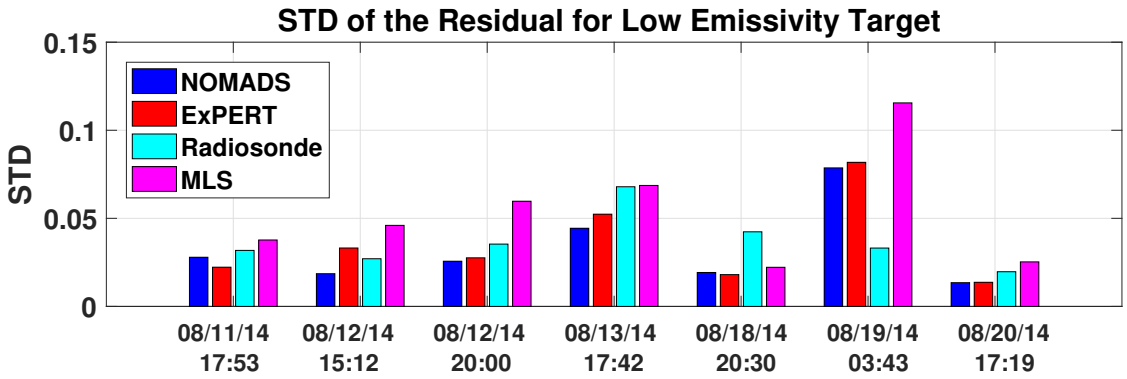

(b) STD of the Residual for the Low Emissivity Target

Figure 6. Figure showing the RMS error and STD of the residual for the low emissivity target for all data cubes. The NOMADS atmosphere resulted in less error and STD of the residual than MLS in all cases and less error than the radiosonde data in all cases. ExPERT returned less RMS error than MLS in all cases except for one, and less STD of the residual than MLS in all cases.

found by calculating the STD of the averaged values and dividing that by the square root of the number of samples. The mean RMS errors of NOMADS and ExPERT are below that of MLS and are outside the uncertainty range. It is also worth noting that the NOMADS RMS error and STD are less than the radiosonde error and outside the uncertainty ranges.

The radiosonde data is generally treated as being the truth atmosphere, but there are two reasons that the NOMADS and ExPERT atmospheres resulted in less RMS error and less STD of the residual. The first reason is time difference between the radiosonde balloon launch and the data collection. Figures 7a and 7b plot the RMS

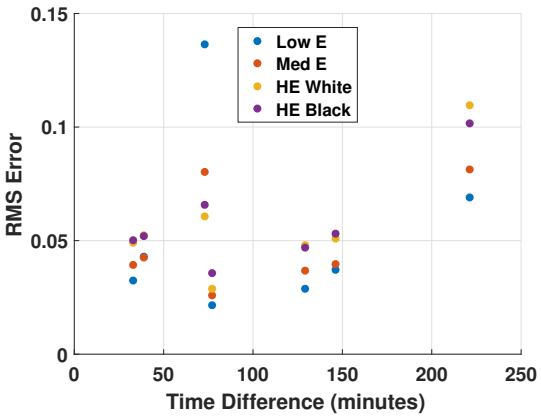

(a) RMS Error

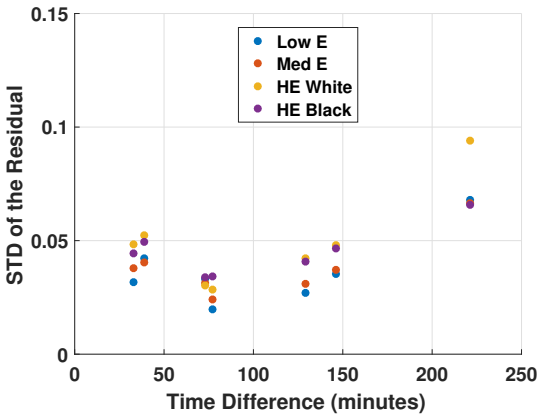

(b) STD of the Residual

Figure 7. These plot the RMS error and STD of the residual of the radiosonde atmospheres against the time difference between the radiosonde launch and the hyperspectral data collection. There is an obvious trend of error increase after the time difference is greater than about two hours. The large RMS error at about 70 minutes time difference in Figure 7a is the night time collection (refer to Figure 6).

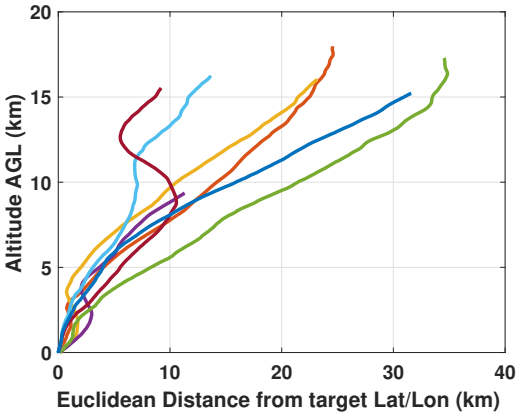

(a) Distance up to 20km in altitude

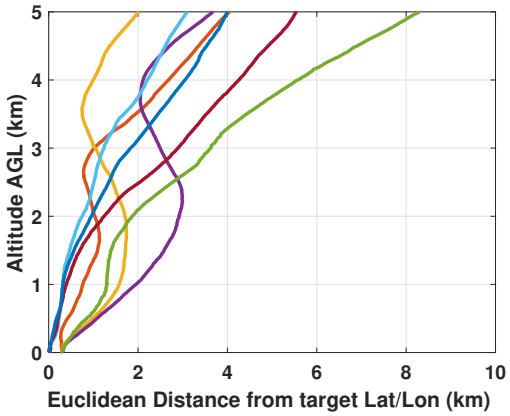

(b) Distance up to 5km in altitude

Figure 8. These plot the distance in kilometers of the radiosonde balloon from the vertical profile at the target latitude and longitude. Figure 8a shows the distance at all altitudes collected by the radiosonde balloon and Figure 8b shows the distances up to five kilometers to provide a better picture for the most important part of the atmosphere. Over half of the balloons are at least two kilometers away from the target latitude/longitude at only three kilometers in altitude.

error and STD of the residual of the radiosonde atmospheres against the time difference between the radiosonde launch and the hyperspectral data collection. There is an obvious trend of error increase after the time difference is greater than about two hours. The large RMS error at about 70 minutes time difference in Figure 7a is the night time collection (refer to Figure 6).

The second reason is that the radiosonde balloon drifts away from the vertical above the target as it rises. Figure 8 plots the distance in kilometers of the radiosonde balloon from the vertical profile at the target latitude and longitude. Figure 8a shows the distance at all altitudes collected by the radiosonde balloon and Figure 8b shows the distances up to five kilometers to provide a better picture for the most important part of the atmosphere. Over half of the balloons are at least two kilometers away from the target latitude/longitude at only three kilometers in altitude. The atmosphere can change dramatically in two horizontal kilometers, and that would increase errors in the retrieved emissivity.

Comparing the iterated TUD spectra in Figure 9 to the first guess spectra in Figure 3 immediately shows a tighter grouping of the TUD spectra after iteration. It is expected that because the TUD spectra are very similar the extracted emissivity will also be close to each other. Figure 10 and Tables 3 and 4 confirm this by showing that the RMS error and the STD of the residual between the extracted emissivities using the different atmospheric profiles is statistically insignificant.

It should be noted that the STD of the residual for the first guess NOMADS atmosphere and the iterated NOMADS are the same. Many target detection algorithms use a correlation statistic, so this result suggests that the performance between the first guess NOMADS and iterated NOMADS atmospheres would be similar. More study is required to make any conclusions on this topic.

Because all of the extracted emissivities were very similar after iteration, the

rate at which each atmospheric profile converged to its optimal solution was analyzed. The Nelder-Mead minimization parameter was recorded at each iteration for all atmospheres and all data cubes. The results from two data cubes are presented in Figure 11. Figure 11a shows that the NOMADS atmosphere converges around twenty iterations and the radiosonde converges around seven. This result was not repeated throughout the other data cubes as can be seen in Figure 11b. The data cube taken on 8/12/2014 at 17:53 was the only instance of significant difference between atmospheres in the number of iterations it took to converge to an optimal solution.

The Nelder-Mead minimization technique is not suited well for this type of study because of the way that it searches for the global minimum. The progressive steps in the Nelder-Mead approach are small, so a different minimization function may lend itself better to this metric [20]. The data shows a large decrease in error within the first few iterations as in Figure 11b, so an approach that combines the Nelder-Mead with a gradient based iteration technique may prove useful. Although this may work in most cases, there is still risk of finding a local minimum after only a few iterations with Nelder-Mead for data similar to Figure 11a.

Figure 12 shows how the atmospheric profiles were adjusted for measured ground temperature and dew point. It can be seen in Figures 12a and 12b that the temperature profiles retain their original lapse rate but the ground temperatures are all equal. Figures 12c and 12d show that the dew point profiles also retain their general shape while the dew point at the surface is adjusted. Figure 13 plots the extracted emissivities using ground weather with and without iterating. Comparing Figure 13a to Figure 4a shows a degradation in performance caused by adjusting the profiles for known ground weather.

The reason for the performance degradation is likely to lie in the way that the atmospheric water content was adjusted. The large mismatch in extracted emissivity

in the water absorption bands at the edges of the spectra in Figure 13a are indicative of incorrect water content. MODTRAN takes water profiles as relative humidity but the adjustment, Equation 23, requires water content in PPMV. In order to adjust the profiles, the relative humidity was converted to PPMV. There is no existing closed form solution from this conversion, so an approximation with empirically derived constants was used. MODTRAN can receive water content in PPMV but it produces an error if the water exceeds 9999 PPMV, a possible scenario at the surface. Therefore, relative humidity was used to circumvent this error.

Tables 3 and 4 show the mean RMS error and STD of the residual of the extracted emissivity spectra over all targets and data cubes of the initial atmospheric compensation, iterated, initial using ground weather, and iterated using ground weather. Using measured ground weather to adjust the temperature and water content had a negative effect on all atmospheres.

Table 1. This table displays the RMS error for all data cubes and all targets. It also presents the mean RMS error over the targets for each data cube and the mean over all targets and data cubes. The green boxes represent the lowest error out of the four atmospheres. The NOMADS atmosphere returned the lowest mean RMS error over all targets and data cubes and had the highest number of green boxes. ExPERT atmosphere returned the second lowest mean RMS error and had the second most green boxes.

		NOMADS	ExPERT	Radiosonde	MLS
8/11/2014	*Low Emissivity Target*	0.0286	0.0227	0.0325	0.0377
17:53	*Medium Emissivity Target*	0.0313	0.0283	0.0394	0.0413
9000ft.	*High Emissivity Black Target*	0.0414	0.0321	0.0493	0.0585
	High Emissivity White Target	0.0411	0.0397	0.0501	0.0505
	Mean	**0.0356**	**0.0307**	**0.0428**	**0.0470**
8/12/2014	*Low Emissivity Target*	0.0192	0.0341	0.0286	0.0527
15:12	*Medium Emissivity Target*	0.0250	0.0283	0.0368	0.0565
9000tf.	*High Emissivity Black Target*	0.0325	0.0365	0.0480	0.0746
	High Emissivity White Target	0.0366	0.0333	0.0468	0.0603
	Mean	**0.0283**	**0.0330**	**0.0401**	**0.0610**
8/12/2014	*Low Emissivity Target*	0.0259	0.0275	0.0371	0.0611
20:00	*Medium Emissivity Target*	0.0294	0.0274	0.0398	0.0610
9000ft.	*High Emissivity Black Target*	0.0381	0.0354	0.0508	0.0809
	High Emissivity White Target	0.0401	0.0381	0.0529	0.0681
	Mean	**0.0334**	**0.0321**	**0.0452**	**0.0678**
8/13/2014	*Low Emissivity Target*	0.0529	0.0799	0.0691	0.0852
17:42	*Medium Emissivity Target*	0.0377	0.0411	0.0812	0.0615
9000ft.	*High Emissivity Black Target*	0.0498	0.0481	0.1095	0.0816
	High Emissivity White Target	0.0424	0.0380	0.1018	0.0698
	Mean	**0.0457**	**0.0518**	**0.0904**	**0.0745**
8/18/2014	*Low Emissivity Target*	0.0194	0.0182	0.0428	0.0251
20:30	*Medium Emissivity Target*	0.0302	0.0294	0.0424	0.0317
6000ft.	*High Emissivity Black Target*	0.0318	0.0303	0.0522	0.0381
	High Emissivity White Target	0.0430	0.0507	0.0521	0.0437
	Mean	**0.0311**	**0.0322**	**0.0474**	**0.0346**
8/19/2014	*Low Emissivity Target*	0.0894	0.1226	0.1365	0.1167
03:43	*Medium Emissivity Target*	0.0765	0.0981	0.0803	0.1119
3000ft.	*High Emissivity Black Target*	0.0618	0.0680	0.0606	0.1001
	High Emissivity White Target	0.0584	0.0677	0.0657	0.0969
	Mean	**0.0715**	**0.0891**	**0.0858**	**0.1064**
8/20/2014	*Low Emissivity Target*	0.0135	0.0142	0.0215	0.0252
17:19	*Medium Emissivity Target*	0.0315	0.0358	0.0261	0.0358
3000ft.	*High Emissivity Black Target*	0.0243	0.0253	0.0286	0.0333
	High Emissivity White Target	0.0642	0.0762	0.0356	0.0575
	Mean	**0.0334**	**0.0378**	**0.0280**	**0.0380**
Mean Over All Targets and Data Cubes		**0.0399**	**0.0438**	**0.0542**	**0.0613**
Uncertainty of the Mean		**0.0033**	**0.0048**	**0.0051**	**0.0047**

Table 2. This table displays the STD of the residual for all data cubes and all targets. It also presents the mean STD over the targets for each data cube and the mean over all targets and data cubes. The green boxes represent the lowest STD out of the four atmospheres. The NOMADS atmosphere resulted in the lowest mean STD over all data cubes and targets, while the ExPERT atmosphere had the most green boxes. The differences in mean STD between NOMADS and ExPERT are within the uncertainty, while the difference between NOMADS and radiosonde is not within uncertainty, and MLS in not within the uncertainty for any other atmosphere.

		NOMADS	ExPERT	Radiosonde	MLS
8/11/2014	*Low Emissivity Target*	0.0279	0.0223	0.0318	0.0377
17:53	*Medium Emissivity Target*	0.0302	0.0279	0.0378	0.0406
9000ft.	*High Emissivity Black Target*	0.0406	0.0304	0.0484	0.0582
	High Emissivity White Target	0.0358	0.0345	0.0444	0.0423
	Mean	**0.0336**	**0.0288**	**0.0406**	**0.0447**
8/12/2014	*Low Emissivity Target*	0.0186	0.0332	0.0271	0.0460
15:12	*Medium Emissivity Target*	0.0242	0.0271	0.0311	0.0416
9000tf.	*High Emissivity Black Target*	0.0283	0.0320	0.0423	0.0710
	High Emissivity White Target	0.0313	0.0277	0.0409	0.0441
	Mean	**0.0256**	**0.0300**	**0.0353**	**0.0507**
8/12/2014	*Low Emissivity Target*	0.0257	0.0276	0.0354	0.0597
20:00	*Medium Emissivity Target*	0.0279	0.0267	0.0370	0.0550
9000ft.	*High Emissivity Black Target*	0.0342	0.0313	0.0482	0.0792
	High Emissivity White Target	0.0342	0.0313	0.0466	0.0535
	Mean	**0.0305**	**0.0292**	**0.0418**	**0.0619**
8/13/2014	*Low Emissivity Target*	0.0444	0.0524	0.0679	0.0687
17:42	*Medium Emissivity Target*	0.0369	0.0412	0.0664	0.0584
9000ft.	*High Emissivity Black Target*	0.0386	0.0419	0.0938	0.0730
	High Emissivity White Target	0.0329	0.0315	0.0659	0.0491
	Mean	**0.0382**	**0.0417**	**0.0735**	**0.0623**
8/18/2014	*Low Emissivity Target*	0.0193	0.0181	0.0424	0.0222
20:30	*Medium Emissivity Target*	0.0284	0.0268	0.0405	0.0296
6000ft.	*High Emissivity Black Target*	0.0304	0.0278	0.0522	0.0331
	High Emissivity White Target	0.0351	0.0324	0.0495	0.0358
	Mean	**0.0283**	**0.0263**	**0.0461**	**0.0302**
8/19/2014	*Low Emissivity Target*	0.0786	0.0818	0.0331	0.1155
03:43	*Medium Emissivity Target*	0.0742	0.0781	0.0314	0.1115
3000ft.	*High Emissivity Black Target*	0.0505	0.0658	0.0301	0.0876
	High Emissivity White Target	0.0492	0.0647	0.0340	0.0858
	Mean	**0.0632**	**0.0726**	**0.0322**	**0.1001**
8/20/2014	*Low Emissivity Target*	0.0135	0.0137	0.0197	0.0253
17:19	*Medium Emissivity Target*	0.0241	0.0252	0.0242	0.0295
3000ft.	*High Emissivity Black Target*	0.0197	0.0186	0.0286	0.0330
	High Emissivity White Target	0.0376	0.0356	0.0342	0.0429
	Mean	**0.0237**	**0.0233**	**0.0267**	**0.0327**
Mean Over All Targets and Data Cubes		**0.0347**	**0.0360**	**0.0423**	**0.0546**
Uncertainty of the Mean		**0.0028**	**0.0033**	**0.0030**	**0.0046**

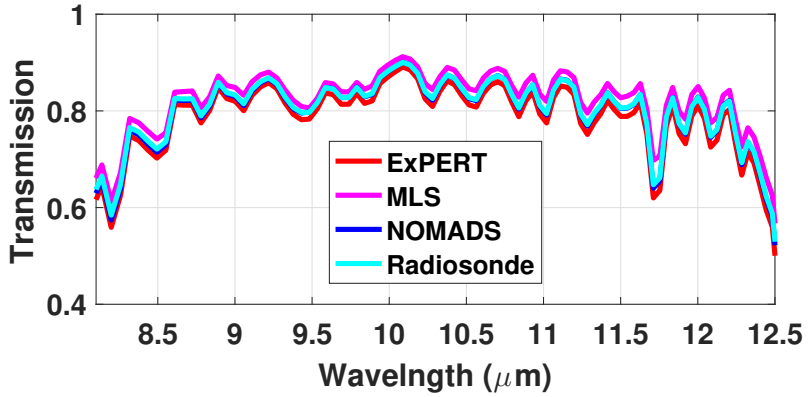

(a) Transmission

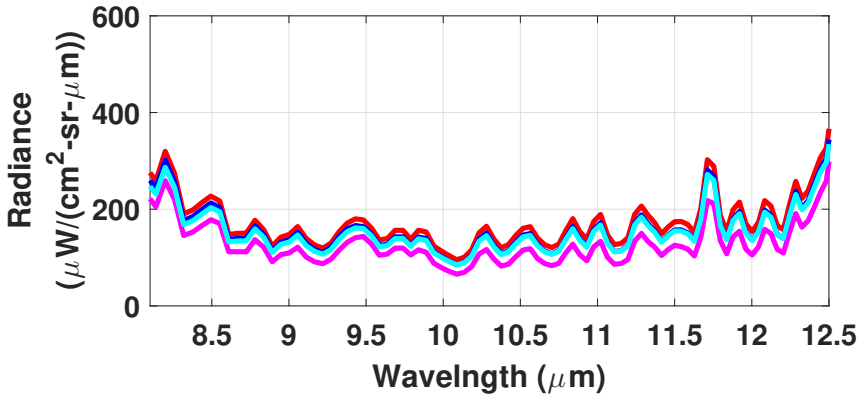

(b) Upwelling Radiance

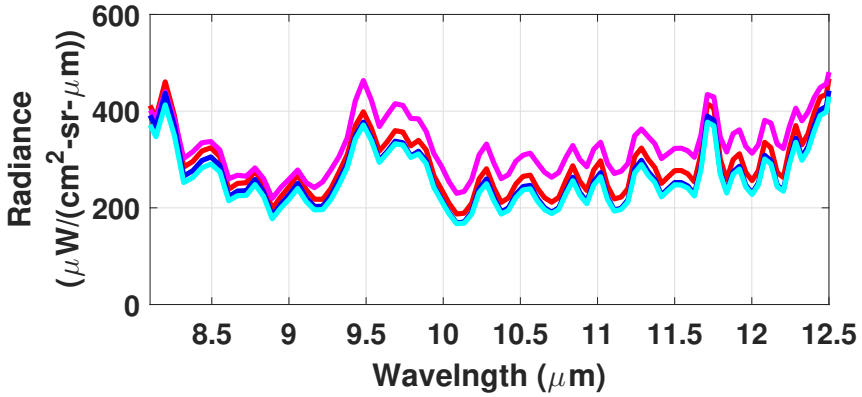

(c) Downwelling Radiance

Figure 9. Figures 9a, 9b, and 9c plot the iterated spectra for the transmission, upwelling, and downwelling radiance respectively. The transmission spectra for all atmospheres is fairly consistent, while the radiance spectra are more spread out. The iteration changes water content at two altitudes in the profiles but cannot change the total water column, leading to slightly different radiance spectra.

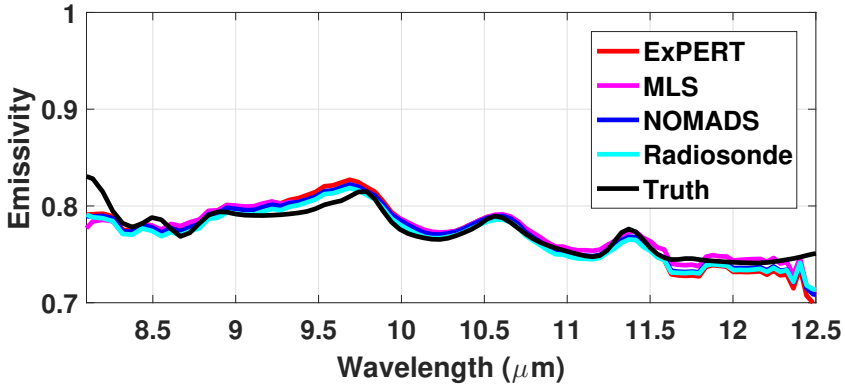

Figure 10. Figure showing the extracted emissivity of the low emissivity target after iteration. All of the extracted spectra are close to the truth spectra.

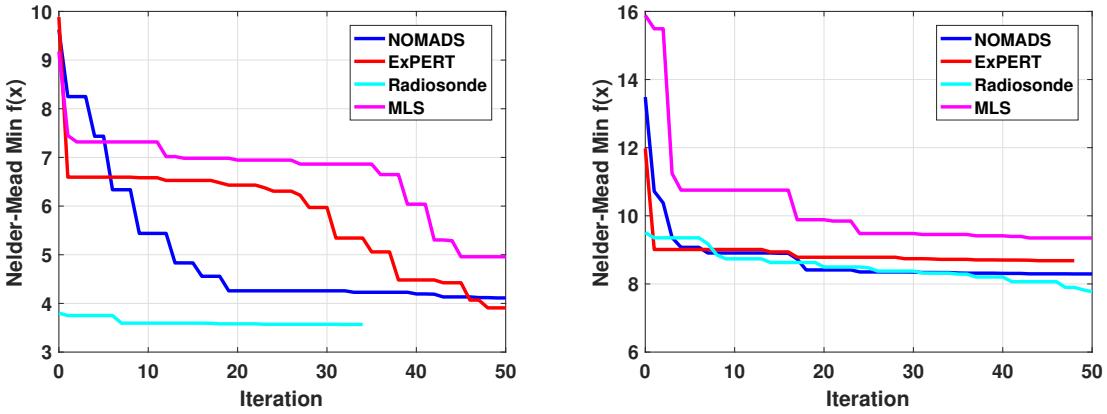

(a) 8/12/2014 at 17:53 (b) 8/12/2014 at 20:00

Figure 11. This figure shows the mean RMS error at each iteration number for the diverse pixels matched to the forward modeled library spectra. This data was used to try and determine if any atmosphere converged to an optimal solution with less iterations than another. Figure 11a shows the NOMADS atmosphere converging around twenty iterations and the radiosonde converging around seven. This result was not shown in the other data however, as can be seen in Figure 11b.

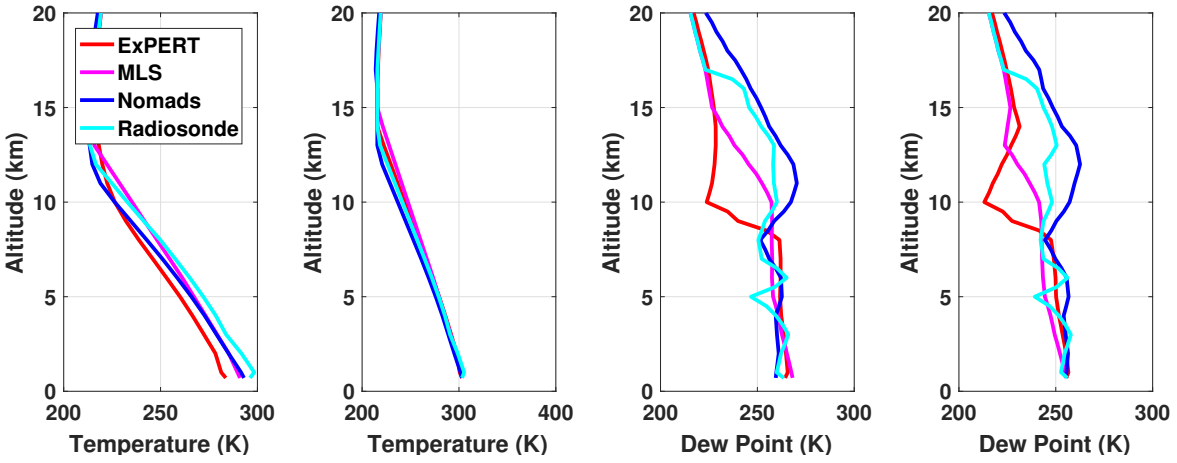

(a) Temperature (b) Temperature, Adjusted (c) Dew Point (d) Dew Point, Adjusted

Figure 12. Figure showing the atmospheric profiles after ground weather adjustments. It can be seen that the adjusted temperature profiles share the same ground temperature but retain their original lapse rate. The dew point plot also retains its original shape after being adjusted for the measured surface water content.

Table 3. This table displays the mean RMS error of the extracted emissivity spectra over all targets and data cubes of the initial atmospheric compensation, iterated, initial using ground weather, and iterated using ground weather. Iteration brings the error for all of the atmospheres together so that the difference in errors is statistically insignificant. Using measured ground weather to adjust the temperature and water content had a negative effect on all atmospheres.

	NOMADS	ExPERT	Radiosonde	MLS
Mean, First Guess, No Weather Adjustment	0.0399	0.0438	0.0542	0.0613
Uncertainty of the Mean	0.0033	0.0048	0.0051	0.0047
Mean, Iterated, No Weather Adjustment	0.0186	0.0182	0.0196	0.0167
Uncertainty of the Mean	0.0043	0.0043	0.0047	0.0041
Mean, First Guess, Using Weather Adjustment	0.0624	0.0799	0.0787	0.0914
Uncertainty of the Mean	0.0044	0.0053	0.0078	0.0050
Mean, Iterated, Using Weather Adjustment	0.0511	0.0625	0.0633	0.0585
Uncertainty of the Mean	0.0040	0.0049	0.0044	0.0049

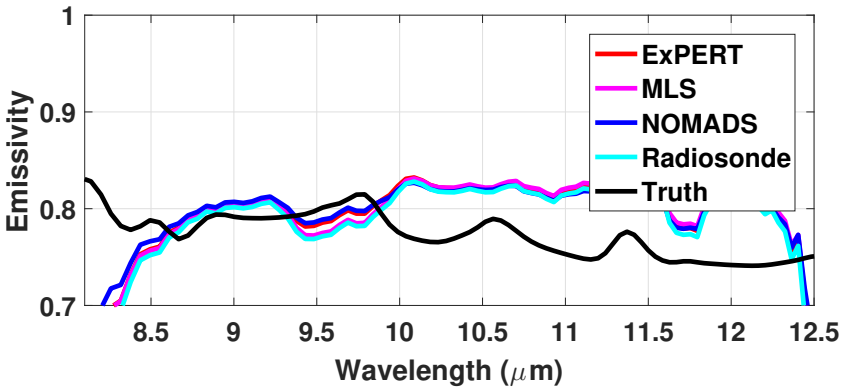

(a) Low Emissivity Target With Ground Adjustments

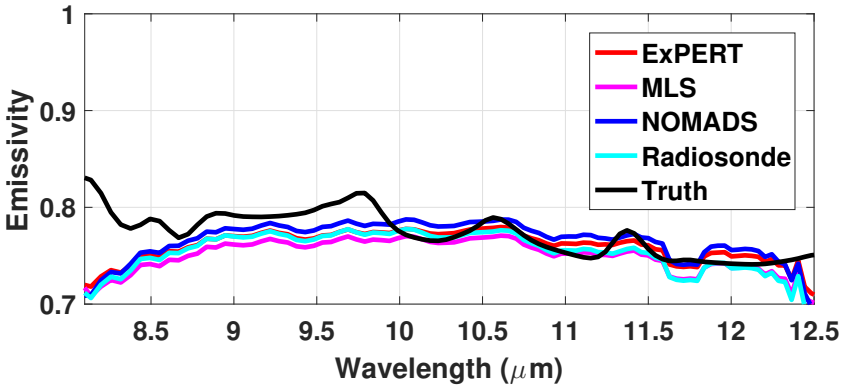

(b) Low Emissivity Target Iterated and With Ground Adjustments

Figure 13. Figure showing the extracted emissivity of the low emissivity target before and after iteration and using ground measurements. Adjusting the atmospheric profiles with known ground weather hurt the performance of all atmospheric profiles. It is suspected that there was an error in atmospheric water content unit conversions using empirical formulas. The drop in emissivity at the edges of the band in Figure 13a indicates a large error in the amount of water in the atmosphere.

Table 4. This table displays the mean STD of the residual of the extracted emissivity spectra over all targets and data cubes of the initial atmospheric compensation, iterated, initial using ground weather, and iterated using ground weather. Iteration brings the STD for all of the atmospheres together so that the difference is statistically insignificant. There is no statistical difference between the STD of the NOMADS first guess and the NOMADS iterated results. Using measured ground weather to adjust the temperature and water content had a negative effect on all atmospheres.

	NOMADS	ExPERT	Radiosonde	MLS
Mean, First Guess, No Weather Adjustment	0.0347	0.0360	0.0423	0.0546
Uncertainty of the Mean	0.0028	0.0033	0.0030	0.0046
Mean, Iterated, No Weather Adjustment	0.0349	0.0344	0.0371	0.0320
Uncertainty of the Mean	0.0024	0.0019	0.0022	0.0013
Mean, First Guess, Using Weather Adjustment	0.0584	0.0727	0.0714	0.0832
Uncertainty of the Mean	0.0041	0.0053	0.0065	0.0051
Mean, Iterated, Using Weather Adjustment	0.0396	0.0474	0.0485	0.0454
Uncertainty of the Mean	0.0026	0.0042	0.0034	0.0041

V. Conclusions

The results show that using the NOMADS or ExPERT atmospheric profiles as a first guess consistently provided improved emissivity estimates over using MLS for atmospheric compensation. In terms of RMS error and STD of the residual, NOMADS and ExPERT generally outperformed the results obtained using radiosonde data and MLS. The radiosonde presented larger RMS error and STD of the residual because of time differences between the balloon launch and the data collection and because of latitude and longitude balloon drift during its ascent.

The atmospheres were iterated with a Nelder-Mead minimization fifty times which resulted in no statistical difference between the four atmospheric profiles. An interesting result shown by the iterations was that the NOMADS first guess and NOMADS iterated atmospheres resulted in the same STD of the residual. Although there is not enough information here to make conclusions about target detection performance, this result should be examined in a target detection scenario in future work.

There was no definitive answer to the question posed about which atmospheric profile would converge to an optimal solution in the fewest iterations. There was only one out of seven data sets that suggested that the NOMADS atmosphere would converge around twenty iterations. The remaining six data sets gave no indication that any of the atmospheres converged faster than another. It was determined that the Nelder-Mead minimization was not appropriate for this type of analysis. A combination of Nelder-Mead and gradient based solutions could likely produce a more interesting result.

Using known ground weather to adjust the temperature and water content of the atmospheric profiles caused a degradation in performance for all atmospheres. The reason for this is suspected to lie in how the water content adjustment was performed. In these simulations, MODTRAN used relative humidity as the input for atmospheric

water content. In order to adjust this, the relative humidity was converted to parts-per-million by volume using an empirically modeled equation. The profile was then adjusted using Equation 23 and converted back to relative humidity. Any error in this conversion equation would be doubled, and could result in larger RMS error and STD. The low emissivity at the edges of the band in the extracted spectra indicate that there is an error in the amount of atmospheric water. This could be avoided in future studies by using parts-per-million by volume as the input to MODTRAN.

There are many things that can be done in the future to confirm and widen the validity range of these results. Performing this study over a larger number of data cubes and weather conditions would help to confirm these conclusions. Using different standard model atmospheres and data cubes collected over other geological locations would widen the validity range of these results.

Bibliography

1. U.S. Standard Atmosphere Supplements, 1962. Technical report, U.S. Government Printing Office, Washington, D.C., 1962.

2. U.S. Standard Atmosphere Supplements, 1966. Technical report, U.S. Government Printing Office, Washington, D.C., 1966.

3. U.S. Standard Atmosphere Supplements, 1976. Technical report, U.S. Government Printing Office, Washington, D.C., 1976.

4. S. M. Adler-Golden, P. Conforti, M. Gangon, P. Tremblay, and M. Chamberland. Long-wave infrared surface reflectance spetra retrieved from Telpos Hyper-Cam imagery. In *Proc. SPIE, vol. 9088*. SPIE, June 2014.

5. Brent Bartlett and John R. Schott. Atmospheric compensation in the presence of clouds: an adaptive empirical line method (aelm) approach. *Journal of Applied Remote Sensing*, 3(1):033507–033507–16, 2009.

6. A. Berk, P.K. Acharya, L.S. Berstein, G.P. Anderson, P. Lewis, J.H. Chetwynd, K. Cady-Pereira, S. Boukabara, and P. D. Brown. Atmospheric radiative transfer modeling: a summary of the AER codes. In *Short Communication, J. Quant. Spectrosc. Radiat. Transfer, 91*, pages 233–244, 2005.

7. A. Berk, P. Conforti, R. Kennett, T. Perkins, F. Hawes, and J. van den Bosch. MODTRAN6: a major upgrade of the MODTRAN radiative transfer code. In *Proc. SPIE, vol. 9088*. SPIE, June 2014.

8. Alexander Berk and Tim C. Perkins. Physics of the MODTRAN5 band model algorithm [Supplemental Material]. Burlington, MA, July 2016. Spectral Sciences, Inc.

9. L. S. Bernstein, s. m. Adler-Golden, R. L. Sundberg, R. Y Levine, T. C. Perkins, A. Berk, J. Ratkowski, A., Felde G., and M. L. Hoke. A new method for atmospheric correction and aerosol optical property retrieval for VIS-SWIR multi- and hyperspectral imaging sensors: QUAC (QUick atmospheric correction), 2005.

10. Marvin Boonmee, John R. Schott, and David W. Messinger. Land surface temperature and emissivity retrieval from thermal infrared hyperspectral imagery, 2006.

11. C. C. Borel. Surface emissivity and temperature retrieval for a hyperspectral sensor. In *Geoscience and Remote Sensing Symposium Proceedings, 1998, IGARSS '98. 1998 IEEE International*, volume 1, pages 546–549 vol.1, 1998.

12. Robert J. DiStasio, Jr. and Ronald G. Resmini. Atmospheric compensation of thermal infrared hyperspectral imagery with the emissive empirical line method and the in-scene atmospheric compensation algorithms: a comparison, 2010.

13. Michael T. Eismann. *Hyperspectral Remote Sensing*. SPIE, P.O. Box 10 Bellingham, Washington, 2012.

14. Alexander Berk et al. Algorithm theoretic basis document (ATBD) for next generation MODTRAN. pages 14–22, Burlington, MA, June 2016. Spectral Sciences, Inc.

15. S.T. Fiorino, R.M. Randall, M.F. Via, and J.L. Burley. Validation of a UV-to-RF high-specral-resolution atmospheric boundary layer characterization tool. In *J. Appl. Meteor. Climatol. Vol 53, No. 1*, pages 136–156, 2014.

16. S.T. Fiorino, R.J.Bartell, M.J. Krizo, G.L. Caylor, K.P. Moore, and S.J. Cusumano. Validation of a worldwide physics-based high-spectral resolution atmospheric characterization and propagation package for UV to RF wavelengths. In *Proc. SPIE 7090, 70900I*. SPIE Optics and Photonics, August 2008.

17. Steven T. Fiorino, Richard J. Bartell, Matthew J. Krizo, Gregory L. Caylor, Kenneth P. Moore, Thomas R. Harris, and Salvatore J. Cusumano. A first principles atmospheric propagation and characterization tool: the laser environmental effects definition and reference (LEEDR). volume 6878, pages 68780B–68780B–12. Spectral Sciences, Inc., 20008.

18. Alaxander F. H. Goetz. Three decades of hyperspectral remote sensing of the earth: A personnal view. *Remote Sensing of Environment*, 113:5–16, 2009.

19. D. Gu, A. R. Gillespie, A. B. Kahle, and F. D. Palluconi. Autonomous atmospheric compensation (aac) of high resolution hyperspectral thermal infrared remote-sensing imagery. *IEEE Transactions on Geoscience and Remote Sensing*, 38(6):2557–2570, Nov 2000.

20. Tamara G. Kolda, Robert Michael Lewis, and Virginia Torczon. Optimization by direct search: New perspectives on some classical and modern methods. *SIAM review*, 45(3):385–482, 2003.

21. D. A. Landgrebe. Multispectral land sensing: where from, where to? pages 414–421.

22. Michael W. Matthew, Steven M. Adler-Golden, Alexander Berk, Gerald W. Felde, Gail P. Anderson, David Gorodetzky, Scott E. Paswaters, and Margaret Shippert. Atmospheric correction of spectral imagery: evaluation of the flaash algorithm with aviris data, 2003.

23. Gilbert N. Plass. Models for spectral band absorption. *Optical Society of America*, 48(10):690–703, 1958.

24. Glenn K. Rutledge, Jordan Alpert, and Wesley Ebisuzaki. NOMADS: A climate and weather model archive at the national oceanic and atmospheric administration. *Bulletin of the American Meteorological Society*, 87(3):327–341, 2006.

25. U. Schumann, Fahey D. W., M. Wendisch, and J. L. Brenguier.

26. Pierre V. Villeneuve and Alan D. Stocker. Oblique projection retrieval of the atmosphere (opra), 2002.

27. Nathan P. Wurst, Joseph Meola, and Steven T. Fiorino. Improved atmospheric characterization for hyperspectral exploitation. volume 10198, pages 101980B–101980B–7, 2017.

28. Nathan P. Wurst, Joseph Meola, and David L. Perry. Measurement and modeling of longwave infrared directional downwelling spectral radiance. In *Proc. SPIE, vol. 9611*. SPIE, 2015.

29. Stephen J. Young, B. Robert Johnson, and John A. Hackwell. An in-scene method for atmospheric compensation of thermal hyperspectral data. *Journal of Geophysical Research*, 107(D24, 4774), 2002.

REPORT DOCUMENTATION PAGE

Form Approved
OMB No. 0704–0188

1. REPORT DATE *(DD–MM–YYYY)*	2. REPORT TYPE	3. DATES COVERED *(From — To)*
10–01–2015	Master's Thesis	Oct 2015 — June 2017

4. TITLE AND SUBTITLE

IMPROVED ATMOSPHERIC CHARACTERIZATION FOR HYPERSPECTRAL EXPLOITATION

5a. CONTRACT NUMBER

5b. GRANT NUMBER

5c. PROGRAM ELEMENT NUMBER

6. AUTHOR(S)

Nathan P. Wurst

5d. PROJECT NUMBER

5e. TASK NUMBER

5f. WORK UNIT NUMBER

7. PERFORMING ORGANIZATION NAME(S) AND ADDRESS(ES)

Air Force Institute of Technology
Graduate School of Engineering and Management (AFIT/EN)
2950 Hobson Way
WPAFB OH 45433-7765

8. PERFORMING ORGANIZATION REPORT NUMBER

AFIT-ENP-MS-17-J-014

9. SPONSORING / MONITORING AGENCY NAME(S) AND ADDRESS(ES)

AFRL/RYMT
2241 Avionics Circle
WPAFB OH 45433-7765
Email: nathan.wurst@us.af.mil

10. SPONSOR/MONITOR'S ACRONYM(S)

AFRL/RYMT

11. SPONSOR/MONITOR'S REPORT NUMBER(S)

12. DISTRIBUTION / AVAILABILITY STATEMENT

DISTRIBUTION STATEMENT A:
APPROVED FOR PUBLIC RELEASE; DISTRIBUTION UNLIMITED.

13. SUPPLEMENTARY NOTES

14. ABSTRACT

Airborne hyperspectral imaging (HSI) in the LWIR has shown utility in material detection and identification. This research seeks to determine the most effective methods to perform model-based atmospheric compensation of LWIR HSI data by comparing results obtained from different atmospheric profiles. The standard model for mid-latitude summer (MLS) and radiosonde data are compared to the National Operational Model Archive and Distribution System (NOMADS) numerical weather predictions and the Extreme and Percentile Environmental Reference Tables (ExPERT). The two latter atmospheric profiles are generated using the Laser Environmental Effects Definition and Reference (LEEDR) software. MLS has been a standard starting point for model-based atmospheric compensation codes, but this study tests the effectiveness of starting with a more accurate model of the atmosphere. The results suggest improvements can be obtained using NOMADS and ExPERT when compared to MLS and radiosonde approaches.

15. SUBJECT TERMS

Atmospheric Compensation, LEEDR, LWIR, MODTRAN, Hyperspectral Imaging

16. SECURITY CLASSIFICATION OF:			17. LIMITATION OF ABSTRACT	18. NUMBER OF PAGES	19a. NAME OF RESPONSIBLE PERSON
a. REPORT	b. ABSTRACT	c. THIS PAGE			Dr. Steven Fiorino, AFIT/ENP
U	U	U	U	59	19b. TELEPHONE NUMBER *(include area code)* (937) 785-3636, x4506; steven.fiorino@afit.edu